Ni Layer Fabrication In Various Temperature Of Watts Solution

Basori[1*], Muhd Ridzuan Mansor[2,3], Maman Kartaman Ajiriyanto[4], Rosika Kriswarini[4], Bambang Soegijono[5], Sigit Dwi Yudanto[6], Dwi Nanto[7], Cahaya Rosyidan[8], and Ferry Budhi Susetyo[9]

[1] *Department of Mechanical Engineering, Universitas Nasional, Sawo Manila Street, Jakarta 12520, Indonesia*
[2] *Fakulti Kejuruteraan Mekanikal, Universiti Teknikal Malaysia Melaka, Hang Tuah Jaya, 76100 Durian Tunggal, Melaka, Malaysia*
[3] *Centre for Advanced Research on Energy, Universiti Teknikal Malaysia Melaka, Hang Tuah Jaya, 76100 Durian Tunggal, Melaka, Malaysia*
[4] *Research Center for Nuclear Material and Radioactive Waste Technology - National Research and Innovation Agency, KST B.J. Habibie, Tangerang Selatan, Banten 15314, Indonesia*
[5] *PROUDTEK Lab., Department of Geoscience, Universitas Indonesia, Kampus UI, Depok 16424, Indonesia*
[6] *Research Center for Metallurgy - National Research and Innovation Agency, KST B.J. Habibie, Tangerang Selatan, Banten 15314, Indonesia*
[7] *Department of Physics Education, UIN Syarif Hidayatullah, Ir. H. Djuanda Street, Ciputat 15412, Indonesia*
[8] *Department of Petroleum Engineering, Universitas Trisakti, Kyai Tapa Street, Jakarta 11440, Indonesia*
[9] *Department of Mechanical Engineering, Universitas Negeri Jakarta, Rawamangun Muka Street, Jakarta 13220, Indonesia*
[*] *Corresponding author. E-mail: basori@civitas.unas.ac.id*

Received: Oct. 30, 2023; Accepted: May. 06, 2024

An electrode that produces oxy-hydrogen gas (HHO) through electrolysis, commonly uses stainless steel (SS). Nickel (Ni) electrodeposition over copper (Cu) alloy promises to replace SS in the electrolyte solution for HHO production. Therefore, it needs a deep exploration of electrodeposition Ni over Cu alloy. In the present work, Ni film electrodeposition was conducted at various electrolyte solution temperatures. Watts solution was chosen due to its better performance than other plating bath compositions. The scanning electron microscopy-energy dispersive spectroscopy (SEM-EDS), X-ray diffractometer (XRD), Potentiostat, and hardness apparatus were employed to identify the characteristics of the Ni films over the Cu alloy. An increase in the solution temperature led to an increase in deposition rate, roughness, crystallite size, and transformation of nodules into pyramidal colonies. The high hardness of Ni-15 (Ni films synthesized over the Cu alloy at 15 °C electrolyte solution) is attributed to its smaller crystallite size. The Ni-15 sample has 38 nm of crystallite size and 232.26 HV of hardness. A lower corrosion rate was also found in the Ni-15 sample, about 1.84×10^{-3} mmpy. Therefore, it is recommended that the Ni-15 be selected as an electrode for HHO production because of its higher hardness and lower corrosion rate.

Keywords: Electrodeposition; Watts solution; Structure; Electrochemical behavior; Hardness

http://dx.doi.org/10.6180/jase.202504_28(4).0016

1. Introduction

The increase in daily demand for energy and alternative energy sources happens due to the depletion and growth in the price of fossil fuels [1, 2]. Moreover, the rise in global temperature is gradually influenced by cumulative gas emissions of green houses [3]. Recently, hydrogen has become a clean, sustainable, and renewable power source alternative [4]. Hydrogen fuel cell electric generators do

not emit emissions or cause noise such in traditional automotive vehicles [5].

Electrolysis, thermolysis, and bio-photolysis techniques have the potential to produce oxy-hydrogen gas (HHO) [6]. In comparison to other HHO production methods, the eco-friendly water electrolysis technique is capable of producing high-density hydrogen [7]. Several studies have employed NaCl, NaOH, and KOH as catalysts in the water electrolysis technique [8–10]. Water electrolysis would produce higher HHO production using KOH due to its conductivity than other catalysts [11]. An increase in the KOH concentration would increase HHO production, resulting in a maximum KOH concentration of 0.5 M [12]. Unfortunately, the increase in KOH concentration led to an increase in corrosion rate [13].

SS 304L, 316L, and 430L are common stainless steel (SS) used as electrodes in HHO production through electrolysis [14]. Production cost in 2017 in Argentina for nickel (Ni) electrodes and electrodeposited Ni on SS316L is about $ 1324 and $ 489 per square meter, representing a saving cost at around 63 %. Electrodeposited Ni on the SS 316L considerably decreased the material cost [15]. Therefore, electrodeposited Ni promises to replace SS in the electrolyte solution for HHO production [16].

Hamidah et al. investigated the use of SS 304, SS 316, and copper (Cu) alloy as electrodes in the water electrolysis apparatus and found that Cu alloy has a higher corrosion rate [17]. Ni electrodeposited onto Cu could be promising to enhance corrosion resistance. Yang et al. performed Ni electrodeposition on bare Cu and reported that the formed Ni film successfully protected bare Cu by showing a decreased corrosion rate in the 3.5 % NaCl solution [18].

The Ni film electrodeposition usually uses a Watts solution due to the better performance than other plating bath compositions [19, 20]. Moreover, electrodeposition is commonly conducted at various electrolyte temperatures to achieve better physical and mechanical properties. Jinlong et. al. have conducted Ni electrodeposition onto SS 304 at different temperatures of Watts solution $(20, 50$, and $80°C)$ [21]. They reported that the corrosion rate at the sample deposited at 20°C was less due to the resulting (111) plane of crystal structure. In contrast, Mirzamohammadi et. al. conducted Ni electrodeposition on CK45 steel in Watts solution $(53 \pm 2°C)$, resulting prefer orientation in the (111) plane of crystal structure [22]. Previous research reported, when electrodeposited Ni on Cu alloy in sulfate solution $(10, 25$, and $40°C)$, found the (111) plane of crystal structure dominant in all samples [23]. In a different investigation, the dominant crystal (111) plane was formed by electrodepositing Ni on a Cu-based alloy in a sulfate-borate solution at temperatures of 20 and 50°C [24].

Based on above mentioned statement, the dominant and preferred orientation of the (111) plane of crystal structure depends on temperature, substrate, and solutions. The film's corrosion resistance is related to the surface energy scale [25]. Face center cubic (FCC) metal surface energy is $(111) < (001) < (110)$ plane of crystal structure [26]. The specimen with the (111) plane of crystal structure offers better corrosion resistance properties regardless of its crystallite size [27]. Thus, this study aims to produce Ni films that are electrodeposited onto the Cu alloy with the dominant orientation (111) plane of crystal structure for the HHO electrodes. The mass increase after electrodeposition was measured using the mass balance to find the deposition rate. Scanning electron microscopy-energy dispersive spectroscopy (SEM-EDS), X-ray diffractometer (XRD), and hardness tests were used to investigate Ni film properties. The electrochemical behavior of Ni films in the KOH solution was studied using the potentiostat.

2. Material and experimental methods

2.1. Material and electroplating procedure

In this experiment, we employed pure Ni rod as the anode and Cu alloy (Al2.97wt.%, Ni 2.01wt.%, and Cu balance) as the substrate. Watts solutions $(300\,g/1NiSO_4.6H_2O, 45\,g/l\ NiCl_2.6H_2O$ and $45\,g/1H_3BO_3$) were prepared as electrolytes solutions using an analytical grade from Merck manufacturer. The Ni film was electrodeposited for 60 minutes at a current density of 10 mA/cm^2 using a DC power supply (MDB PS-305DM). Electrodeposition of Ni film was conducted in various temperatures $(15, 30$, and $45°C)$ and was titled as $Ni-15$, Ni-30, and Ni-45, respectively. The schematic electrodeposition of Ni is presented in Fig. 1.

2.2. Samples characterizations

The deposition rate of various samples could be calculated using the following equation [28].

$$v = \frac{1000 \times \Delta m}{\rho \times S \times t} \tag{1}$$

Where v is the deposition rate $(\mu m/h)$, Δm is a mass increment of Ni film over Cu alloy after electrodeposition (g), t is the electrodeposition duration (h), ρ is the Ni density (8.9 g/cm^3), and S is the Cu alloy substrates area.

The Ni film's surface morphology and elemental distribution were observed using an SEM-EDS from Oxford Instruments. A PANalytical XRD (Cu $k\alpha$ $\lambda = 1.5406$ Å) scanned from 20 to 100° was used to evaluate the Ni film's structure. The MATLAB software analyzed the roughness

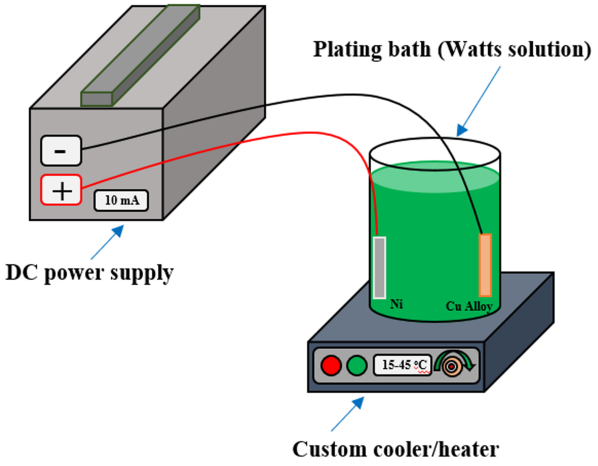

Fig. 1. Schematic electrodeposition of Ni onto Cu alloy.

of the specimens [29]. The following equation calculated the coefficient of mass variation percentage [30].

$$cv(\%) = \frac{Standard\ deviation}{Average} \times 100 \quad (2)$$

The potentiostat (Gamry Reference 600) investigated electrochemical behavior at room temperature in a 1MKOH solution (Merck). The open circuit potential (OCP) measurement was scanned until the 800 s prior to the potentiodynamic polarization (PP) scan. The measurement of PP was done using a scan rate of 0.001 V/s. Ni film is used as the working electrode (WE), saturated calomel electrode (SCE) is used as the reference electrode (RE), and platinum wire is used as a counter electrode (CE). The value of corrosion current (i_{corr}) and corrosion potential (E_{corr}) was found by the Tafel extrapolation method [31]. Corrosion rate (CR) was found by inserting i_{corr} into the following equation [32].

$$CR(mmpy) = C\frac{M \times i_{corr}}{n \times \rho} \quad (3)$$

Where C is the corrosion rate constant (3.27mmpy), n is the number of electrons involved, ρ is the density (g/cm^3), M is the atomic weight (g/mol), and i_{corr} is the corrosion current density (A/cm^2). Electrochemical impedance spectroscopy (EIS) measurement was performed from $0.05 - 45000$ Hz. EIS measurement outputs can be visualized in Nyquist and Bode plot curves. By fitting the Bode plot curve using the electrical equivalent circuit (EEC), the impedance parameter (R_{ct} and R_s) is obtained.

An FV-300e Vickers hardness tester (1 kg) was used to measure the hardness of the specimen. Five-spot measurements were collected from each specimen to find the average hardness of the film.

3. Result and discussions

3.1. Deposition rate

Fig. 2 shows the deposition rate of various samples. The deposition rates were calculated using equation (1). The deposition rate increases with the electrolyte temperature from 12.22 to 13.15μm/h. This phenomenon means that the deposition rate is dependent on the electrolyte temperature. Chung et. al. conducted an electrodeposition of Ni using an electrolyte solution temperature between -0.15 and 19.85°C. Due to the lower reductive current at low plating bath temperature, the deposition rate decreases as the bath temperature drops. Poor mass transfer conditions at low plating bath temperatures have limited the deposition rate [33]. The poor mass transfer led to a decrease in the deposition rate due to the slow movement of Ni^{2+} from the anode to the cathode [23].

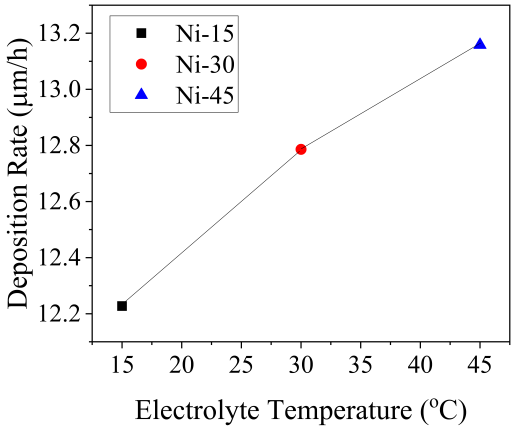

Fig. 2. Deposition rate of Ni films.

3.2. SEM-EDS

Fig. 3 represents the SEM-EDS results of various samples. All Ni films are compact and crack-free, as seen in Fig. 3. Electrodeposition was conducted at 15°C, resulting in a spherical structure morphology. Badarulzaman et. al. reported that nodules were formed during the electrodeposition process using Watts solution at $21 - 22$°C [34]. Moreover, increasing temperature leads to a change in spherical structure to the polygonal texture morphology (Fig. 3 (b) and (c)). This change could probably be due to the fact that nucleation and growth rates increase with a rise in temperature. Tan et. al. found bath temperature slightly affects the nucleation mechanism of electrodeposition [35]. The increased temperature could promote the ion's activity, and their diffusion could be accelerated in the plating bath.

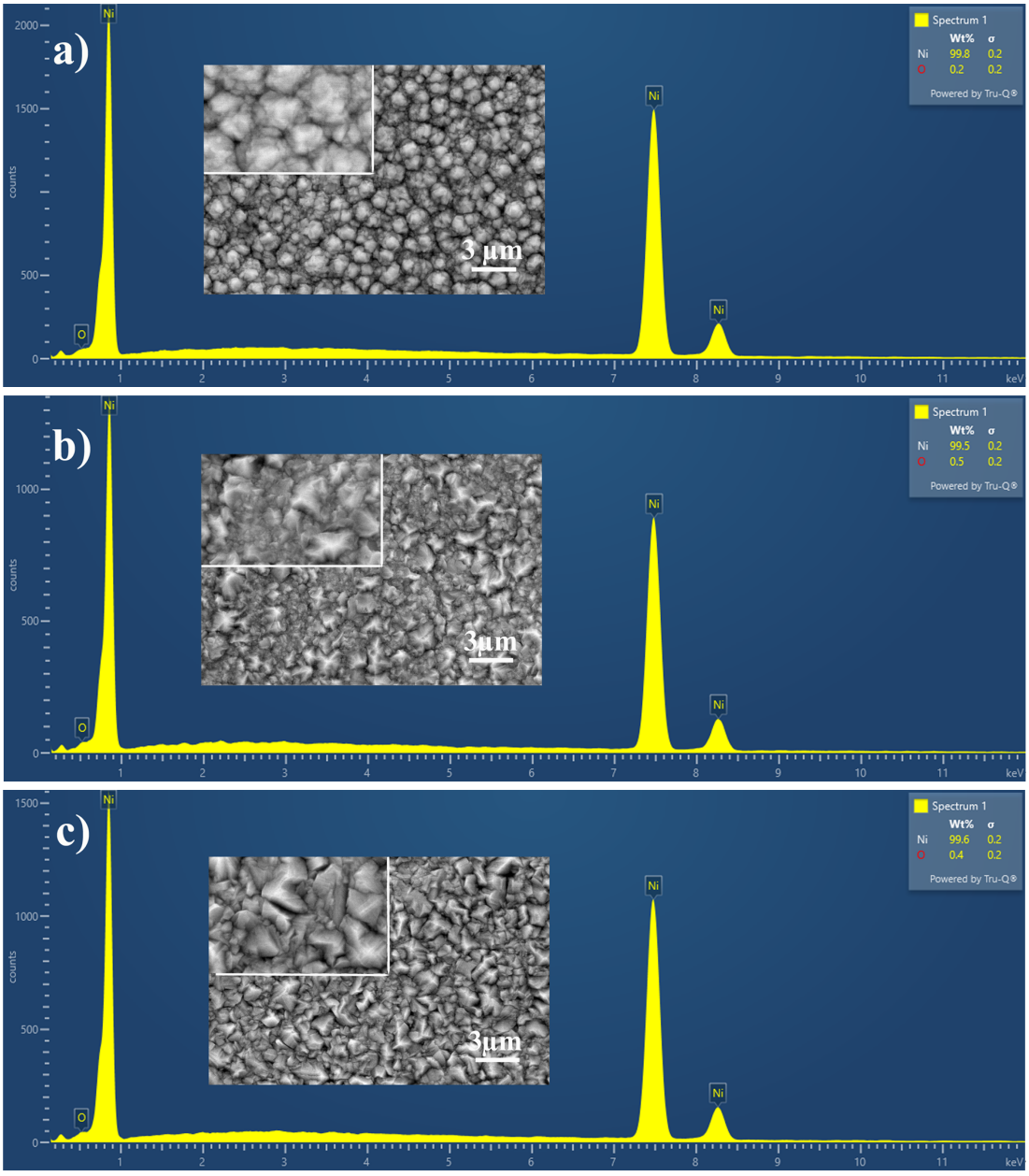

Fig. 3. SEM-EDS investigation a) Ni-15, b) Ni-30 and c) Ni-45.

There are two forms of nucleation of the electrodeposition: (a) Atoms reduced onto the surface of the cathode gather to form a crystal nucleus and then grow to form crystals, and (b) After reaching a specific position and entering the crystal lattice, the reduced atoms diffuse onto the electrode's surface. They continue to grow on the original metal crystal lattice for the case of dislocation into matrix material [35–37].

Compared with the previous research, the deposition rate is 3μm/h, resulting in island-like structure morphology, while the deposition rate is around 6.2 and 7.2μm/h, resulting in nodule form morphology [23]. In the present work, the deposition rate is around 12.2μm/h, resulting in nodule form morphology, while the deposition rate is around 12.8 and 13.15μm/h, resulting in polygonal texture morphology. It can be concluded that the deposition rate $\leq 3\mu$m/h resulted in island-like structure morphology, the deposition rate between 6.2 - 12.2μm/h resulted in nodule form morphology, and the deposition rate $\geq$ 12.8 μm/h resulted in polygonal texture morphology.

Fig. 3 also shows the EDS result of the Ni films. Ni was perfectly deposited onto Cu alloy, presenting a low oxygen

content. Ni-15, Ni-30 and Ni-45 have 0.2, 0.5, and 0.4 wt.% oxygen content, respectively. It is still debated whether oxygen is present on the surface of the Ni film. Previous research has shown that increased electrolyte temperatures reduce the oxygen content when Ni is deposited on a Cu alloy with a sulfate solution [23]. Susetyo et. al. reported carbon and oxygen due to specimen transport and storage before the EDS investigation in another previous study [24]. Xing et. al. also found Ni oxide was easily formed on the Ni surface in the atmosphere at room temperature [38].

The MATLAB software evaluated surface film properties based on SEM results. Fig. 4 illustrates the surface roughness and histogram of the Ni films.

Table 1. Ni film roughness properties.

Sample	Average	Standard deviation	cv (%)
Ni-15	152.29	37.43	24.58
Ni-30	154.77	41.49	26.81
Ni-45	132.60	49.33	37.20

The cv is calculated by Eq. (2) and summarized in Table 1. The surface becomes rougher when the cv is higher. Table 1 shows that the Ni-45 sample has a higher cv, which indicates that the Ni-45 sample has a rough surface. According to Fig. 2, an increase in the temperature of the electrolytes leads to a higher deposition rate. A higher deposition rate increases the nucleation sites and will obtain the rough structure of the sample surface.

Chung et. al. found the morphology of Ni at low-temperature smoother than at high temperatures. Ni film forms at 5,10 , and 15°C, resulting in average roughness of 30.43 , 66.17 , and 78.62 nm, respectively. Ni films were deposited at 5°C has compact clusters. Rough morphologies with more extensive cluster arrangements are seen in 10 and 15°C samples [39]. Jabbar et. al. electrodeposited Ni with a modified Watts bath (adding 0.4 g/1 surfactant and 0.2 g/l graphene), resulting in average roughness 34.2, 91.1, 128, and 151 nm at deposition temperatures 15, 30, 45, and 60°C, respectively [40].

It seems that enhancement of the solution temperature affects the nucleation rate of the Ni electrodeposition. The nucleation rate increases due to the rise of the electrodeposition solution temperature. A higher nucleation rate promotes increased grain growth, which affects higher surface roughness.

3.3. XRD

Fig. 5 shows the diffraction patterns for Ni samples deposited on Cu substrates at 15°C (Ni-15), 30°C(Ni − 30), and 45°C(Ni − 45). The occurrence of phase peaks with indexes plane (111), (200), (220), (311), and (222) at 15°C heating revealed the presence of Ni crystal growth. The Ni phase peaks align with the results of several previous investigations [41–43]. It is obvious that there is an orientation in the plane (200) in the sample heated at 30°C. The insert in Fig. 5 clearly shows the orientation of the plane (200). When the sample is deposited at 45°C, the crystal orientation is also displayed.

The diffraction pattern has an increased intensity value for the diffraction peaks in addition to the plane orientation (200). The Rietveld method was used to refine the diffraction model in order to determine the impact of heating on the crystal growth of Ni [44]. The lattice constant of Ni phase is determined at 0.352 nm based on the refinement results of the diffraction patterns as described in Table 2. These results indicate that the heating method did not cause the lattice distortion of the Ni crystals.

The estimated crystallite size is then determined using the diffraction pattern that results from the refinement. The estimated crystallite size is then determined using the diffraction pattern that results from the refining. The crystallite size for all samples was assessed using the modified Scherrer technique [45–47]. As seen in Fig. 6, the basic idea of the modified Scherrer technique is to construct the $\ln(1/\cos\theta)$ versus ln FWHM (full width at half maximum) curve. The FWHM is expressed in radians. Table 2 lists the FWHM values for each crystal plane in the three samples. For each of the samples Ni-15, Ni-30, and Ni-45, the linear equation results in the curve plot $(1/\cos\theta)$ versus ln FWHM giving an intercept value of -5.6146, -6.3318, and -6.6711 , respectively. The crystallite size values for each sample are obtained from this intercept value, as shown in Table 2. As deposition temperatures increase, crystals grow faster. According to Sen et al., theoretically, the relation between bath temperature rises and crystal growth is linear [41].

Table 2. Crystallographic data for samples Ni-15, Ni-30, and Ni-45.

Source	Ni-15	Ni-30	Ni-45
FWHM (111) (°)	0.2630	0.1611	0.1353
FWHM (200) (°)	0.3360	0.1804	0.1510
FWHM (220) (°)	0.5480	0.3630	0.2710
FWHM (311) (°)	0.8190	0.5170	0.3940
FWHM (222) (°)	0.8600	0.5300	0.4600
Ni, Lattice constants a (nm)	0.3519	0.3517	0.3517
Intercept	-5.6146	-6.3318	-6.6711
D (nm)	38	80	109

Previous research found the crystallite size of Ni films between $27.85 - 41.38$ nm; the Ni films were fabricated us-

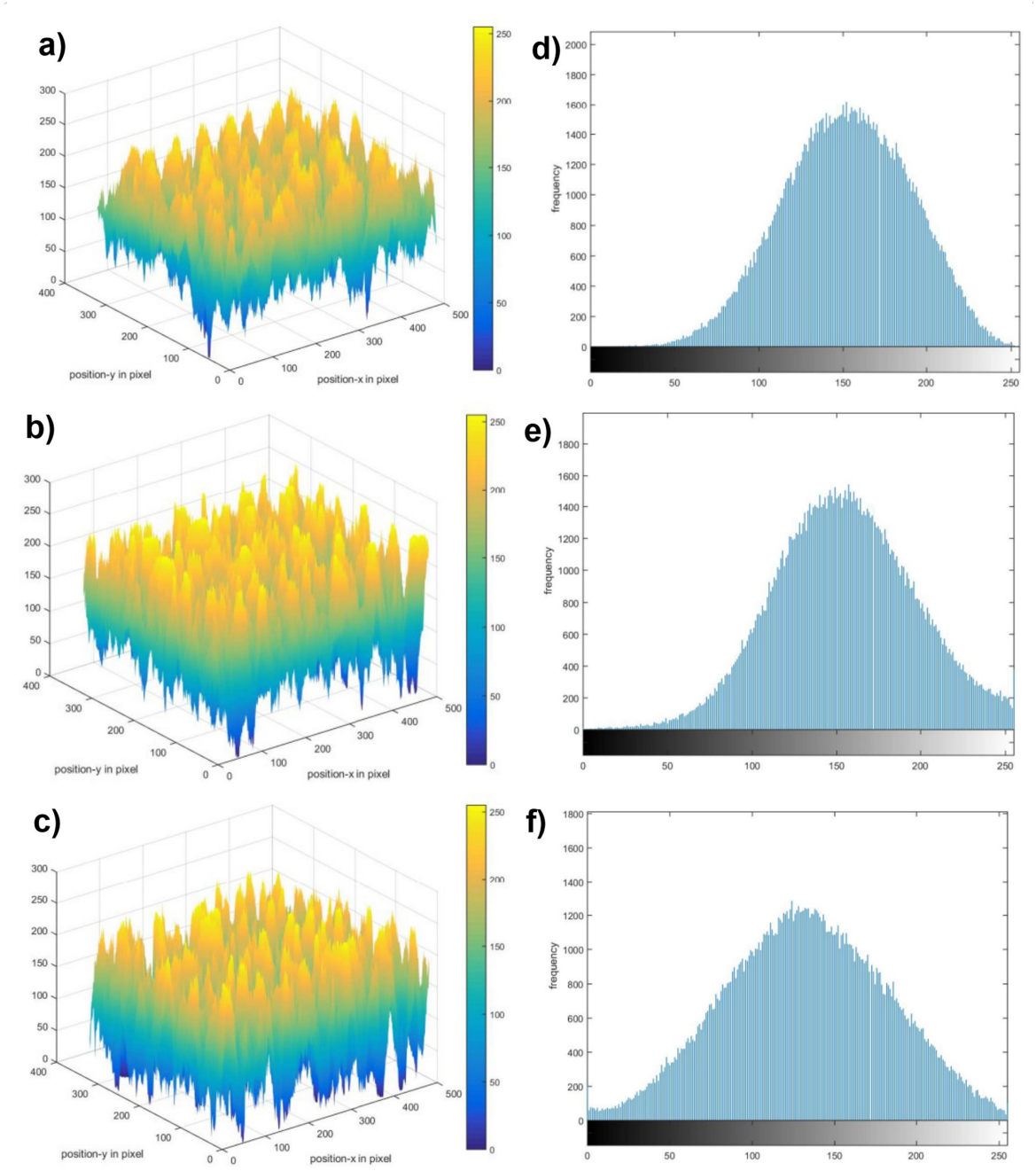

Fig. 4. Roughness analysis result for Ni films a) Ni-15, b) Ni-30, and c) Ni-45 and Histogram analysis result for Ni films d) Ni-15, e) Ni-30, and f) Ni-45.

ing electrodeposition in sulfate electrolyte solution at various solution temperatures (10, 25 and 40°C) [23]. Another report found the crystallite size of Ni films was between 23.4-25.2 nm; the Ni films were fabricated using electrodeposition at a solution temperature range between -0.15 to 19.85°C using a bath containing Ni sulphamate, Ni chloride and boric acid [33]. A larger crystallite size is seen in the present research, probably due to a higher deposition rate (12.22 to 13.15μm/h), while other research has a deposition rate of less than 7.2μm/h.

3.4. OCP

Fig. 7 shows the OCP measurement results in 1 M KOH at room temperature. The initial EOCP of the sample is linearly in line with temperature. All specimens show an increase to a more positive value for reaching a steady state.

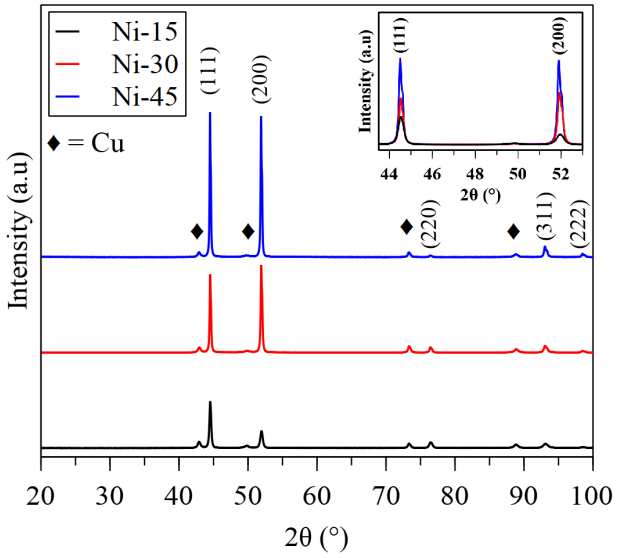

Fig. 5. XRD pattern of sample Ni-15, Ni-30, and Ni-45.

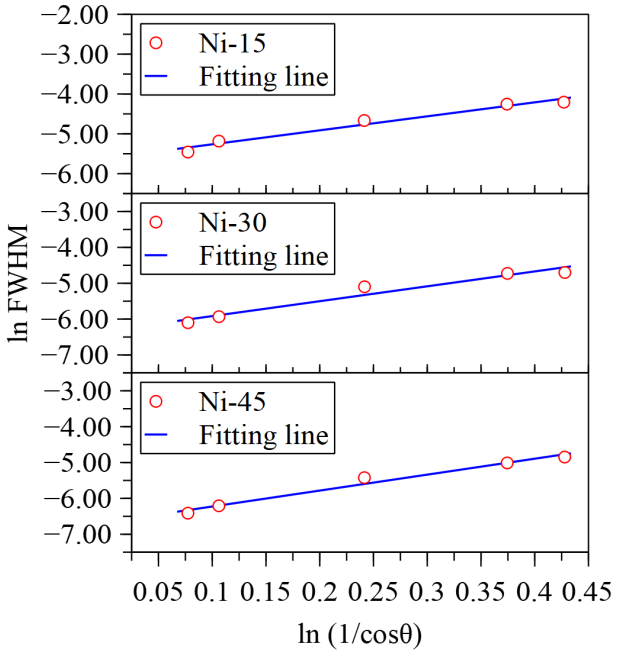

Fig. 6. Plot of $\ln(1/\cos\theta)$ versus ln FWHM.

The OCP values for Ni-15, Ni-30, and Ni-45 at 800 s are -0.300, -0.317, and -0.302 V, respectively. Continuous shifting to a more positive value indicates additional protective and passive film occurring throughout the OCP measurement [24].

3.5. PP

Fig. 8 shows the PP measurement result for all samples. The Ni-30 sample has a prominent active loop, which cannot be seen on other specimens. Krawczyk et al. investigated

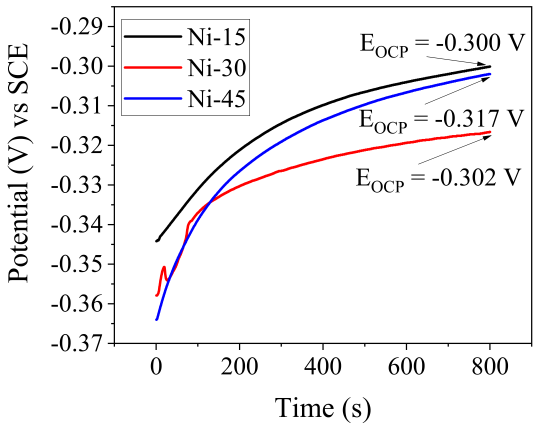

Fig. 7. OCP measurement result.

316L austenitic SS with a chemical composition of (wt.%) 16.7Cr, 10.1Ni, 2.04 Mo, 0.019C, and 0, 049 N in various concentrations of HCl. They found an active loop prominent in samples tested in 1.5 and 0.7MHCl [48]. This behavior indicates oxide forms on the surface (uniform corrosion). Compared to the EDS measurement, the Ni-30 has more oxide in the Ni film, probably causing the formation of a loop.

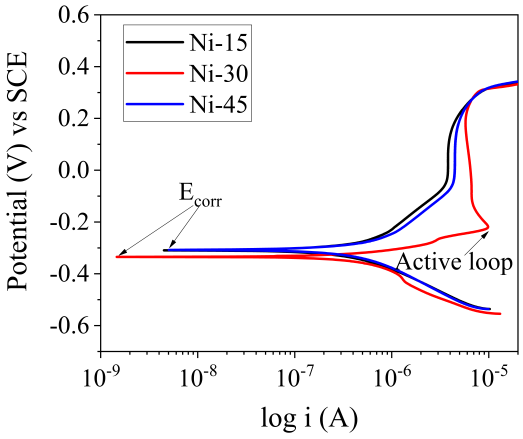

Fig. 8. PP measurement result.

Corrosion is formed due to the interaction of the material with the environment [49]. Based on Table 3, Ni-15 has a lower corrosion rate. The corrosion rate is proportional to the corrosion current, while corrosion potential represents corrosion tendency rather than corrosion resistance [50].

The corrosion rate of the films is closely related to the surface energy scale. Lower surface energy tends to dissolve lower, reducing the corrosion rate [25]. Babich and Pogosov found FCC metal surface energy is (111) <

Table 3. Tafel extrapolation and corrosion rate.

Sample	i_{corr} (A)	E_{corr} (V) vs SCE	CR (mmpy)
Ni − 15	1.6593×10^{-7}	-0.3099	1.84×10^{-3}
Ni − 30	2.6796×10^{-7}	-0.3348	2.98×10^{-3}
Ni − 45	1.8086×10^{-7}	-0.3081	2.01×10^{-3}

(001) < (110) plane of crystal structure [26]. Ni-15 has a dominant (111) plane and, for that reason, has a lower corrosion rate.

Compared to the previous result, which investigated SS 316 L in 50 g/LKOH (room temperature), it shows a higher corrosion rate $(5.613 \times 10^{-3}$mmpy) [13]. Davalos et al. found that SS316 L in aerated 50%NaOH at 25°C has a corrosion rate of 0.368mmpy [51]. Hamidah et al. investigated SS 316, SS 304, and Cu alloy in 30,000 ppm KOH ($\approx$ 29.96 g/l) at 25°C(1008 h exposed time) were found less corrosion rate on SS 304 is 0.042mpy ($\approx 1.1 \times 10^{-3}$mmpy) [17]. Therefore, Cu alloy deposited Ni film would be promising as an electrode for an HHO generator.

3.6. EIS

Fig. 9 represents the Nyquist plot impedance of Ni films measured in KOH solution. The highest capacitive arc is on Ni-15, and the lowest is at the Ni-30 sample. An increase in the capacitive arc radius indicates an increase in the passive film stability, and the increase in the capacitive arc is related to passive film thickening [21]. This condition results in more protection against corrosion attack in the solution [52].

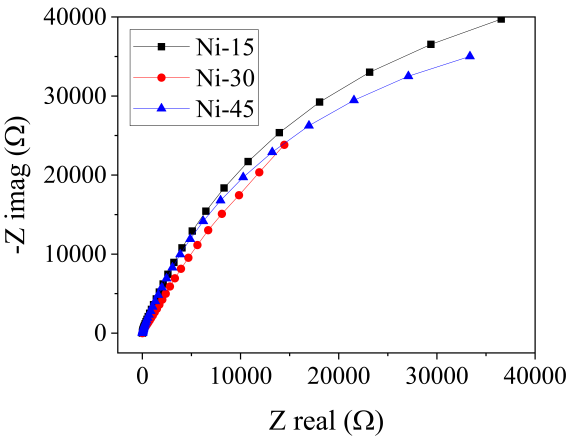

Fig. 9. Nyquist plot of Ni films.

Fig. 10 shows the bode plot of the Ni samples. The bode plot shows the total impedance behavior with respect to the applied frequency. By fitting the curve (Fig. 10) using the EEC, the impedance parameter is obtained. Table 4 shows R_{ct} as polarization or charge transfer resistance and *Rs* as ohmic solution resistance [53].

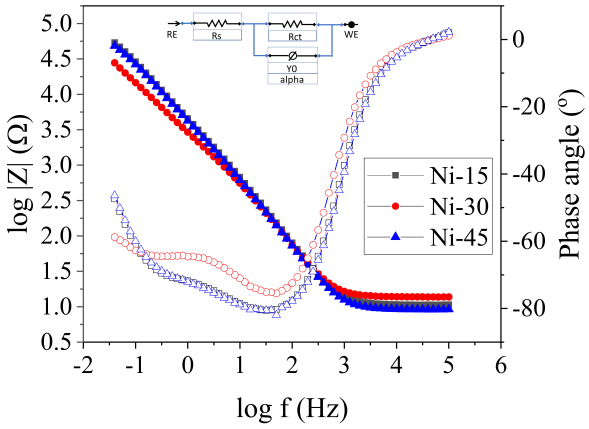

Fig. 10. Bode Plot of Ni films.

The Ni-15 has a higher R_{ct} and capacitive arc than other samples. Zulkafli et. al. have found a decreased capacitive arc, indicating a higher corrosion rate [53]. Zhao et al. reported Ni films with higher R_{ct} promoted the best corrosion resistance [54]. This statement is aligned with Table 3, where there is less corrosion rate at the Ni-15 sample due to higher R_{ct} and a higher capacitive arc.

Table 4. EIS measurement result.

Sample	$R_{ct}(\Omega)$	$R_s(\Omega)$
Ni-15	8.56×10^{-4}	10.22
Ni-30	6.53×10^{-4}	12.64
Ni-45	7.36×10^{-4}	8.78

3.7. Hardness

Fig. 11 shows the hardness between 189.13-232.26 HV, which is in perfect agreement with other studies [34, 55]. The high electrolyte temperature decreases the hardness (Fig. 11) due to the increase in crystallite size. Chung et al. investigated electrodeposition Ni at various temperatures $(-0.15, 4.85, 9.85, 14.85$, and $18.85°C)$, resulting in crystallite sizes 23.42, 23.80, 24.80, 24.90, and 25.23 nm, with hardness 6.37, 6.18, 4.15, 4.11 and 4.01GPa, respectively [33].

Besides crystallite size, the increased nuclei at low temperatures promoted a fine-grain layer, which is beneficial for increasing the hardness [39]. Moreover, Li et al. and Mohanty et al. stated that Ni films with a dominant plane of (111) are more condensed than others [56, 57]. This condition led to more hardness than others due to better crystal arrangement and less porosity. Those two statements are

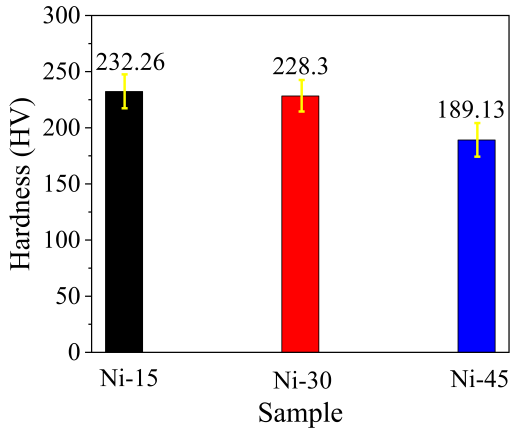

Fig. 11. Hardness of Ni films.

corroborated by the Ni-15 samples having more hardness due to fine-grain and dominant (111) plane.

4. Conclusions

Ni films electrodeposited on Cu alloy were conducted at various electrolyte temperatures. The research conclusions are presented as follows:

1. The rise of the electrolyte solution temperature during the electrodeposition process led to an increase in deposition rate due to more movement of Ni^{2+} from anode to cathode.

2. The electrodeposition process of Ni at 15°C solution temperature resulted in a spherical surface morphology. Increasing the solution temperature changes surface morphology into a polygonal texture. This behavior is probably because nucleation and growth rates increase with a temperature rise.

3. Surface roughness increases due to the rise in electrolyte temperature. An increase in the temperature of the electrolytes leads to a higher deposition rate. A higher deposition rate increases the nucleation sites and will obtain the rough structure of the sample surface.

4. The crystallite size of the Ni film increased (from 37.21 to 108.77 nm) with an increase in electrolyte temperature (from 15 to 45°C) due to an increase in the deposition rate (from 12.22 to 13.15μm/h).

5. The sample was made from the lowest electrolyte solution temperature (15°C), which has higher hardness and less corrosion rate. Higher hardness is reached due to the lowest crystallite size. Meanwhile, a lower corrosion rate was formed due to the dominant (111) plane with a lower surface energy scale. Moreover, the EIS result corroborates this statement: the Ni-15 sample has the highest capacitive arc and charge transfer resistance characteristic, resulting in a lower corrosion rate.

6. Based on the findings in the present research, the Ni-15 sample for the HHO generator electrode is recommended due to its higher hardness and lower corrosion rate.

Acknowledgements

Hibah Kompetitif Universitas Nasional financially supported this project through grant number 012 / SP3K / Ka. Biro Adm. PPM / XI / 2022.

References

[1] C. Tarhan and M. A. Çil, (2021) *"A study on hydrogen, the clean energy of the future: Hydrogen storage methods"* **Journal of Energy Storage *40***: 102676. DOI: 10.1016/j.est.2021.102676.

[2] M. Trongtorkarn, T. Theppaya, M. Luengchavanon, and S. Chowdhry, (2023) *"Wind Tunnel Experiment: Temperature And Starting Torque Affect PMSG Generator When Connected To Vertical Axis Wind Turbine Blade"* **Journal of Applied Science and Engineering (Taiwan) *26***: 207–212. DOI: 10.6180/jase.202302_26(2).0006.

[3] V. V. Pogorelko and A. E. Mayer, (2015) *"Influence of copper inclusions on the strength of aluminum matrix at high-rate tension"* **Materials Science and Engineering A *642***: 351–359. DOI: 10.1016/j.msea.2015.07.009.

[4] S. Lestari, M. Muflihah, R. Kusumawardani, M. Nurhadi, Y. Mangesa, F. I. Ridho, R. Adawiyah, P. Ambarwati, S. Rahma, S. Yuan Lai, and H. Nur, (2022) *"Activated Bledug Kuwu's Clay as Adsorbent Potential for Synthetic Dye Adsorption: Kinetic and Thermodynamic Studies"* **Bulletin of Chemical Reaction Engineering Catalysis *17***: 22–31. DOI: 10.9767/bcrec.17.1.12473.22-31.

[5] A. G. Stern, (2018) *"A new sustainable hydrogen clean energy paradigm"* **International Journal of Hydrogen Energy *43***: 4244–4255. DOI: 10.1016/j.ijhydene.2017.12.180.

[6] C. Acar and I. Dincer, (2019) *"Review and evaluation of hydrogen production options for better environment"* **Journal of Cleaner Production *218***: 835–849. DOI: 10.1016/j.jclepro.2019.02.046.

[7] S. Anwar, F. Khan, Y. Zhang, and A. Djire, (2021) *"Recent development in electrocatalysts for hydrogen production through water electrolysis"* **International Journal of Hydrogen Energy *46***: 32284–32317. DOI: 10.1016/j.ijhydene.2021.06.191.

[8] M. A. El Kady, A. El Fatih Farrag, M. S. Gad, A. K. El Soly, and H. M. Abu Hashish, (2020) *"Parametric study and experimental investigation of hydroxy (HHO) production using dry cell"* **Fuel *282***: 118825. DOI: 10.1016/j.fuel.2020.118825.

[9] M. M. El-Kassaby, Y. A. Eldrainy, M. E. Khidr, and K. I. Khidr, (2016) *"Effect of hydroxy (HHO) gas addition on gasoline engine performance and emissions"* **Alexandria Engineering Journal *55***: 243–251. DOI: 10.1016/j.aej.2015.10.016.

[10] A. C. Yilmaz, E. Uludamar, and K. Aydin, (2010) *"Effect of hydroxy (HHO) gas addition on performance and exhaust emissions in compression ignition engines"* **International Journal of Hydrogen Energy *35***: 11366–11372. DOI: 10.1016/j.ijhydene.2010.07.040.

[11] M. H. Sellami and K. Loudiyi, (2017) *"Electrolytes behavior during hydrogen production by solar energy"* **Renewable and Sustainable Energy Reviews *70***: 1331–1335. DOI: 10.1016/j.rser.2016.12.034.

[12] R. Purwondho, A. Sudrajat, and Handoko, (2021) *"Research on the effect of SS316L electrode plate treatment on HHO gas production performance"* **IOP Conference Series: Earth and Environmental Science *794***: 012021. DOI: 10.1088/1755-1315/794/1/012021.

[13] B. Basori, W. M. F. W. Mohamad, M. R. Mansor, A. Iswadi, M. K. Ajiriyanto, and F. B. Susetyo, (2023) *"Effect of KOH concentration on corrosion behavior and surface morphology of stainless steel 316L for HHO generator application"* **Journal of Electrochemical Science and Engineering *13***: 451–467. DOI: 10.5599/jese.1615.

[14] J. M. Olivares-Ramírez, M. L. Campos-Cornelio, J. Uribe Godínez, E. Borja-Arco, and R. H. Castellanos, (2007) *"Studies on the hydrogen evolution reaction on different stainless steels"* **International Journal of Hydrogen Energy *32***: 3170–3173. DOI: 10.1016/j.ijhydene.2006.03.017.

[15] M. J. Gómez, L. A. Diaz, E. A. Franceschini, G. I. Lacconi, and G. C. Abuin, (2019) *"3D nanostructured NiMo catalyst electrodeposited on 316L stainless steel for hydrogen generation in industrial applications"* **Journal of Applied Electrochemistry *49***: 1227–1238. DOI: 10.1007/s10800-019-01361-8.

[16] M. J. Gomez, E. A. Franceschini, and G. I. Lacconi, (2018) *"Ni and NixCoy Alloys Electrodeposited on Stainless Steel AISI 316L for Hydrogen Evolution Reaction"* **Electrocatalysis *9***: 459–470. DOI: 10.1007/s12678-018-0463-5.

[17] I. Hamidah, A. Solehudin, and A. Setiawan, (2016) *"Effect of variation of kalium hydroxide solution concentration and temperature to the corrosion resistance of AISI 304, AISI 316, and copper alloys in water electrolysis apparatus"* **ARPN Journal of Engineering and Applied Sciences *11***: 972–977.

[18] Z. Yang, X. Liu, and Y. Tian, (2019) *"Fabrication of super-hydrophobic nickel film on copper substrate with improved corrosion inhibition by electrodeposition process"* **Colloids and Surfaces A *560***: 205–212. DOI: 10.1016/j.colsurfa.2018.10.024.

[19] F. B. Susetyo, B. Soegijono, Yusmaniar, M. C. Fajrah, and M. Cahya, (2021) *"Deposition of nickel films on polycrystalline copper alloy with various current densities from watts solution Deposition of Nickel Films on Polycrystalline Copper Alloy with Various Current Densities from Watts Solution"* **AIP Conference Proceedings *2331***: 030017. DOI: 10.1063/5.0041640.

[20] H. Alimadadi, A. B. Fanta, T. Kasama, M. A. Somers, and K. Pantleon, (2016) *"Texture and microstructure evolution in nickel electrodeposited from an additive-free Watts electrolyte"* **Surface Coatings Technology *299***: 1–6. DOI: 10.1016/j.surfcoat.2016.04.068.

[21] L. Jinlong, L. Tongxiang, and W. Chen, (2016) *"Effect of electrodeposition temperature on grain orientation and corrosion resistance of nanocrystalline pure nickel"* **Journal of Solid State Chemistry *240***: 109–114. DOI: 10.1016/j.jssc.2016.05.025.

[22] S. Mirzamohammadi, H. Khorsand, and M. Aliofkhazraei, (2017) *"Effect of different organic solvents on electrodeposition and wear behavior of Ni-alumina nanocomposite coatings"* **Surface Coatings Technology *313***: 202–213. DOI: 10.1016/j.surfcoat.2017.01.025.

[23] S. Syamsuir, B. Soegijono, S. D. Yudanto, B. Basori, M. K. Ajiriyanto, D. Nanto, and F. B. Susetyo, (2023) *"Electrolyte Temperature Dependency of Electrodeposited*

Nickel in Sulfate Solution on the Hardness and Corrosion Behaviors" **International Journal of Engineering Transactions C: Aspects *36***: 1193–1200. DOI: 10.5829/IJE.2023.36.06C.18.

[24] F. B. Susetyo, M. C. Fajrah, and B. Soegijono, (2020) *"Effect of Electrolyte Temperature on Properties of Nickel Film Coated onto Copper Alloy Fabricated by Electroplating"* **e-Journal of Surface Science and Nanotechnology *18***: 223–230. DOI: 10.1380/ejssnt.2020.223.

[25] R. Xin, Y. Luo, A. Zuo, J. Gao, and Q. Liu, (2012) *"Texture effect on corrosion behavior of AZ31 Mg alloy in simulated physiological environment"* **Materials Letters *72***: 1–4. DOI: 10.1016/j.matlet.2011.11.032.

[26] A. V. Babich and V. V. Pogosov, (2009) *"Effect of dielectric coating on the electron work function and the surface stress of a metal"* **Surface Science *603***: 2393–2397. DOI: 10.1016/j.susc.2009.05.036.

[27] M. Hoseini, A. Shahryari, S. Omanovic, and J. A. Szpunar, (2009) *"Comparative effect of grain size and texture on the corrosion behaviour of commercially pure titanium processed by equal channel angular pressing"* **Corrosion Science *51***: 3064–3067. DOI: 10.1016/j.corsci.2009.08.017.

[28] J. Lu, M. Wang, X. Deng, J. Yan, J. Yun, and S. Jiao, (2019) *"Evaluation of K3Fe(CN)6 on Deposition Behavior and Structure of Electroless Copper Plating"* **Electrochemistry *87***: 214–219. DOI: 10.5796/electrochemistry.19-00010.

[29] A. Srivani and M. Anthony Xavior, (2014) *"Investigation of surface texture using image processing techniques"* **Procedia Engineering *97***: 1943–1947. DOI: 10.1016/j.proeng.2014.12.348.

[30] S. Rwawiire, A. Kasedde, I. Nibikora, and G. Wandera, (2014) *"Prediction of polyester/cotton ring spun yarn unevenness using adaptive neuro fuzzy inference system"* **Journal of Textile and Apparel, Technology and Management *8***: 1–12.

[31] X. L. Zhang, Z. H. Jiang, Z. P. Yao, Y. Song, and Z. D. Wu, (2009) *"Effects of scan rate on the potentiodynamic polarization curve obtained to determine the Tafel slopes and corrosion current density"* **Corrosion Science *51***: 581–587. DOI: 10.1016/j.corsci.2008.12.005.

[32] Z. Ahmad. *Principles of corrosion engineering and corrosion control*. Elsevier, 2006, 1–656. DOI: 10.1016/b978-0-7506-5924-6.x5000-4.

[33] C. K. Chung, W. T. Chang, and S. T. Hung, (2010) *"Electroplating of nickel films at ultra low electrolytic temperature"* **Microsystem Technologies *16***: 1353–1359. DOI: 10.1007/s00542-009-0955-6.

[34] N. A. Badarulzaman, A. A. Mohamad, S. Puwadaria, and Z. A. Ahmad, (2010) *"The evaluation of nickel deposit obtained via Watts electrolyte at ambient temperature"* **Journal of Coatings Technology and Research *7***: 815–820. DOI: 10.1007/s11998-010-9271-4.

[35] W. Tan, H. He, Y. Gao, Y. Peng, and X. Dai, (2021) *"Nucleation and growth mechanisms of an electrodeposited Ni–Se–Cu coating on nickel foam"* **Journal of Colloid and Interface Science *600***: 492–502. DOI: 10.1016/j.jcis.2021.05.002.

[36] O. Aaboubi, A. Y. Ali Omar, A. Franczak, and K. Msellak, (2015) *"Investigation of the electrodeposition kinetics of Ni-Mo alloys in the presence of magnetic field"* **Journal of Electroanalytical Chemistry *737***: 226–234. DOI: 10.1016/j.jelechem.2014.10.014.

[37] E. Beltowska-Lehman, (2002) *"Electrodeposition of protective Ni-Cu-Mo coatings from complex citrate solutions"* **Surface and Coatings Technology *151-152***: 440–443. DOI: 10.1016/S0257-8972(01)01613-9.

[38] W. Xing, S. Qiao, X. Wu, X. Gao, J. Zhou, S. Zhuo, S. B. Hartono, and D. Hulicova-Jurcakova, (2011) *"Exaggerated capacitance using electrochemically active nickel foam as current collector in electrochemical measurement"* **Journal of Power Sources *196***: 4123–4127. DOI: 10.1016/j.jpowsour.2010.12.003.

[39] C. K. Chung, W. T. Chang, C. F. Chen, and M. W. Liao, (2011) *"Effect of temperature on the evolution of diffusivity, microstructure and hardness of nanocrystalline nickel films electrodeposited at low temperatures"* **Materials Letters *65***: 416–419. DOI: 10.1016/j.matlet.2010.10.064.

[40] A. Jabbar, G. Yasin, W. Q. Khan, M. Y. Anwar, R. M. Korai, M. N. Nizam, and G. Muhyodin, (2017) *"Electrochemical deposition of nickel graphene composite coatings effect of deposition temperature on its surface morphology and corrosion resistance"* **RSC Advances *7***: 31100–31109. DOI: 10.1039/c6ra28755g.

[41] R. Sen, S. Das, and K. Das, (2011) *"The effect of bath temperature on the crystallite size and microstructure of Ni-CeO2 nanocomposite coating"* **Materials Characterization *62***: 257–262. DOI: 10.1016/j.matchar.2011.01.013.

[42] A. Ul-Hamid, A. Quddusa, H. Saricimena, and H. Dafallaa, (2015) *"Corrosion behavior of coarse- and fine-grain Ni coatings incorporating NaH2PO4.H2O inhibitor treated substrates"* **Materials Research *18***: 20–26. DOI: 10.1590/1516-1439.253114.

[43] G. Cheng, Q. Bai, C. Si, W. Yang, C. Dong, H. Wang, Y. Gao, and Z. Zhang, (2015) *"Nickel oxide nanopetal-decorated 3D nickel network with enhanced pseudocapacitive properties"* **RSC Advances *5***: 15042–15051. DOI: 10.1039/c4ra15556d.

[44] A. C. Larson and R. B. V. Dreele, (2004) *"General Structure Analysis System (GSAS)"*: 1–224.

[45] A. Monshi, M. R. Foroughi, and M. R. Monshi, (2012) *"Modified Scherrer Equation to Estimate More Accurately Nano-Crystallite Size Using XRD"* **World Journal of Nano Science and Engineering *2***: 154–160. DOI: 10.4236/wjnse.2012.23020.

[46] S. D. Yudanto, S. A. Chandra, R. Roberto, D. P. Utama, V. O. Herlina, and Lusiana, (2022) *"Phase and electrical properties of Ca3Co4O9 ceramic prepared by a citrate sol-gel route"* **Journal of Ceramic Processing Research *23***: 287–291. DOI: 10.36410/jcpr.2022.23.3.287.

[47] S. Kamila and V. R. Venugopal, (2017) *"Synthesis and structural analysis of different CuO nano particles"* **International Journal of Applied Science and Engineering *14***: 133–146. DOI: 10.6703/IJASE.2017.14(3).133.

[48] B. Krawczyk, P. Cook, J. Hobbs, and D. L. Engelberg, (2017) *"Corrosion behavior of cold rolled type 316L stainless steel in HCl-containing environments"* **Corrosion *73***: 1346–1358. DOI: 10.5006/2415.

[49] Q. Li, M. G. Lee, J. Che, Y. C. Kan, and C. T. Chiu, (2018) *"Mechanical properties and corrosion resistance of cement concrete containing sea sand or sea water"* **International Journal of Applied Science and Engineering *15***: 199–210. DOI: 10.6703/IJASE.201812_15(3).199.

[50] G. Aydin and A. Yazici, (2019) *"Effect of quenching and tempering temperature on corrosion behavior of boron steels in 3.5 wt.% NaCl solution"* **International Journal of Electrochemical Science *14***: 2126–2135. DOI: 10.20964/2019.03.22.

[51] R. D. Monteiro, J. V. D. Wetering, B. Krawczyk, and D. L. Engelberg, (2019) *"Corrosion Behaviour of Type 316L Stainless Steel in Hot Caustic Aqueous Environments"* **Metals and Materials International *26***: 630–640. DOI: 10.1007/s12540-019-00403-2.

[52] N. Xu, D. K. Sarkar, X. G. Chen, and W. P. Tong, (2016) *"Corrosion performance of superhydrophobic nickel stearate/nickel hydroxide thin films on aluminum alloy by a simple one-step electrodeposition process"* **Surface Coatings Technology *302***: 173–184. DOI: 10.1016/j.surfcoat.2016.05.050.

[53] R. Zulkafli, N. K. Othman, N. Yaakob, F. K. Sahrani, and M. Al-Furjan, (2023) *"Electrochemical Studies of Microbiologically Influenced Corrosion on API 5L X65 by Sulfate-Reducing Bacteria in CO2 Environments"* **Evergreen *10***: 601–607. DOI: 10.5109/6782167.

[54] H. Zhao, L. Liu, J. Zhu, Y. Tang, and W. Hu, (2007) *"Microstructure and corrosion behavior of electrodeposited nickel prepared from a sulphamate bath"* **Materials Letters *61***: 1605–1608. DOI: 10.1016/j.matlet.2006.07.178.

[55] V. F. Lins, E. S. Cecconello, and T. Matencio, (2008) *"Effect of the current density on morphology, porosity, and tribological properties of electrodeposited nickel on copper"* **Journal of Materials Engineering and Performance *17***: 741–745. DOI: 10.1007/s11665-008-9205-9.

[56] C.-q. Li, X.-h. Li, Z.-x. Wang, and H.-j. Guo, (2007) *"Nickel electrodeposition from novel citrate bath"* **Transactions of Nonferrous Metals Society of China *17***: 1300–1306. DOI: 10.1016/s1003-6326(07)60266-0.

[57] U. S. Mohanty, B. C. Tripathy, S. C. Das, and V. N. Misra, (2005) *"Effect of thiourea during nickel electrodeposition from acidic sulfate solutions"* **Metallurgical and Materials Transactions B *36***: 737–741. DOI: 10.1007/s11663-005-0077-1.